Nanostructure-Mediated Phase Evolution in Lithiation/Delithiation of Co_3O_4

Yu Fu[a]‡, Xuyun Guo[b]‡, Zhenglong Xu[c], Guangming Zhao[b], Chao Xu[b], Ye Zhu[b]*, Limin Zhou[d]*

[a]Department of Mechanical Engineering, The Hong Kong Polytechnic University, Hung Hom, Kowloon, Hong Kong, China.

[b]Department of Applied Physics, Research Institute for Smart Energy, The Hong Kong Polytechnic University, Hung Hom, Kowloon, Hong Kong, China.

[c]Department of Industry and Systems Engineering, The Hong Kong Polytechnic University, Hung Hom, Kowloon, Hong Kong.

[d]School of System Design and Intelligent Manufacturing, Southern University of Science and Technology, Xueyuan Road 1088, Shen Zhen, Guang Dong, China.

ABSTRACT

Nanostructured transition metal oxides have been under intensive investigation for their tantalizing potential as anodes of next-generation lithium-ion batteries (LIBs). However, the exact mechanism for nanostructures to influence the LIB performance remains largely elusive. In this work, we discover the nanostructure-mediated lithiation mechanism in Co_3O_4 anodes using *ex situ* transmission electron microscopy (TEM) and X-ray diffractometry: While Co_3O_4 nanosheets exhibit a typical two-step conversion reaction (from Co_3O_4 to CoO and then to Co^0), Co_3O_4 nanoarrays can go through a direct conversion from Co_3O_4 to Co^0 at a high discharge rate. Such nanostructure-dependent lithiation can be rationalized by the slow lithiation kinetics intrinsic to Co_3O_4 nanoarrays, which at a high discharge rate may cause local accumulation of lithium to initiate a one-step Co_3O_4-to-Co^0 conversion. Combined with the larger volume change observed in Co_3O_4 nanoarrays, the slow lithiation kinetics can lead to inhomogeneous expansion with large stress developed at the reaction front, which can eventually cause structure failure and irreversible capacity loss, as explicitly observed by *in situ* TEM as well as galvanostatic discharge-charge measurement. Our observation resolves the nanostructure-dependent lithiation mechanism of Co_3O_4, and provides important insights into the interplay among lithiation kinetics, phase evolution and lithium storage performance which can be translated into electrode design strategies for next generation LIBs.

1. INTRODUCTION

Rechargeable lithium ion batteries (LIBs) have governed applications such as portable devices and are regarded as the most promising power sources for electric vehicles and grid applications.[1-2] Transition metal oxides (TMOs) have gained significant attention since Poizot, et al.[3-4] demonstrated their feasibility as conversion electrode materials for LIBs, and have been proposed as prospective anodes due to their capability of incorporating more than one Li per metal atom, thus delivering much higher electrochemical capacities than those of conventional graphite anodes.[5-6] Among TMO materials, Co_3O_4 has attracted extensive interest due to its high theoretical capacity.[7-8] However, its large volume expansion/contraction during lithiation/delithiation leads to electrode pulverization and the loss of particle contact, which results in a large irreversible capacity loss and poor cycling stability. Despite intensive efforts to overcome the volume expansion and to improve battery performance by developing nanostructured Co_3O_4[9-10] (nanowire,[11] graphene composite,[12] nanocage,[13] etc.[14-16]), the dynamic process that occurs during lithiation/delithiation of various Co_3O_4 nanostructures is still under debate with lots of inconsistencies in literature.[10-15]

Since Thackeray, et al.[17] reported on the intercalation-conversion reaction pathway during the electrochemical lithiation of Co_3O_4, study on the multi-step reaction mechanism has been widely undertaken. However, the detailed process of the conversion reaction in Co_3O_4 remains controversial in literature. Guo, et al.[18] found that the CoO phase forms as the intermediate phase during the conversion from Co_3O_4 to Co^0 using *ex situ* X-ray Diffractometry (XRD) on Co_3O_4 anode at different discharge states. Yuk, et al.[19] also revealed the CoO phase as the initial conversion product of Co_3O_4, followed by the formation of Co^0 using graphene

liquid cell electron microscopy. On the other hand, distinct from the two step Co_3O_4-to-CoO and CoO-to-Co^0 conversion reactions, a direct conversion between Co_3O_4 and Co^0 was observed by Su, et al.,[20] which complicates the lithiation reaction mechanism of Co_3O_4. They studied the reaction kinetics of Co_3O_4 particles using annular dark-field scanning transmission electron microscopy (ADF-STEM) and observed metallic Co^0 phase directly forming from the intercalated $Li_xCo_3O_4$ phase at various discharge rates. Likewise, Lee, et al.[21] observed a direct conversion from Co_3O_4 to Co^0 through *in situ* X-ray absorption fine structure (XAFS) analysis. The direct conversion from Co_3O_4 to Co^0 has also been observed by others.[22-23] Such a controversy about the conversion reaction pathways reflects the complex lithiation mechanism in Co_3O_4, which was first revealed by Tarascon, et. al.[24] by demonstrating that low charge rates or small grains are beneficial for the formation of CoO while high charge rates or large grains favor the formation of $Li_xCo_3O_4$. However, Tarascon's work only revealed the competition between the intercalation and conversion processes without addressing the direct one-step Co_3O_4-to-Co^0 conversion, and thus did not resolve the above controversy in literature.

In this work, we compare the microscopic lithiation/delithiation behaviors of Co_3O_4 anodes with two distinct nanostructures, nanoarrays and nanosheets, using *in situ* and *ex situ* TEM, consolidated by XRD and LIB performance measurements. We discover the dependence of lithiation mechanism on the Co_3O_4 nanostructure as well as the discharge rate, and identified the favorable lithiation conditions for both two-step and one-step conversion reactions. The observed nanostructure-dependent lithiation is underpinned by lithiation kinetics intrinsic to Co_3O_4 nanostructures, which further leads to different structural and cycling stability in LIB anodes. Our results not only resolve the existing controversy on the Co_3O_4 lithiation mechanism in literature, but also shed light on the optimal nanostructure to achieve better LIB performance.

2. EXPERIMENTAL SECTION

Preparation of carbon cloth (CC)-based Co_3O_4 nanosheets and CC-based Co_3O_4 nanoarrays. CC-based Co_3O_4 nanosheets were synthesized according to the following method. Specifically, $Co(NO_3)_2 \cdot 6H_2O$ and 2-methylimidazole were separately dissolved in two beakers of methanol. After continuous stirring for 1 h at room temperature, the two kinds of methanol solutions were then quickly mixed. After the immersion of an oxidized CC (CC-O) in the mixed solution and reaction for 24 h, the reacted CC-O was removed. After rinsing three times with methanol, the reacted CC was heated for 12 h in an oven at 60 °C, and was then heat treated in a furnace at 500 °C for 1 h. Thus, CC-based Co_3O_4 nanosheets were obtained. CC-based Co_3O_4 nanoarrays were synthesized according to the method reported previously.[25] In detail, $Co(NO_3)_2 \cdot 6H_2O$, NH_4F and urea were separately dissolved in a 50 mL Teflon-lined autoclave, followed by the immersion of CC. After reaction, the reacted CC was removed and washed with deionized water before being heated for 12 h in an oven at 60 °C and was subsequently taken to heat treatment at 450 °C for 1 h. Thus, CC@Co_3O_4 nanoarrays were obtained. The measurements of mass loading of Co_3O_4 nanoarrays and nanosheets on CC were performed using the Agilent 725 inductively coupled plasma atomic emission spectrometry (ICP-AES). The average areal mass loading of CC@Co_3O_4 nanosheets and CC@Co_3O_4 nanoarrays were 0.89 and 1.88 mg cm^{-2}, respectively.

Electrode Fabrication and Cell Assembly. Both CC-based Co_3O_4 nanosheets and CC-based Co_3O_4 nanoarrays were cut into 1 cm^2 disks and used directly as anode electrodes without a binder or conductive additive. The electrolyte solution was ethylene carbonate/diethylene carbonate (1:1 v/v) with 1 M LiPF$_6$. Both types of electrodes were assembled in a two-electrode

cell configuration versus Li metal foil counter electrode in an argon-filled glove box, with oxygen and water content below 1 ppm.

Characterizations. The surface morphologies of CC-based Co_3O_4 nanosheets and CC-based Co_3O_4 nanoarrays were characterized by scanning electron microscopy (SEM; TESCAN VEGA3). X-ray diffraction (XRD) patterns were collected on an X-ray diffractometer (XRD; Rigaku Smartlab 9 kW, Cu target). The CR2032 coin-type cells based on CC-based Co_3O_4 nanosheet and CC-based Co_3O_4 nanoarray electrodes were tested in galvanostatic mode at 500 µA cm^{-2} within a voltage range of 0.01 to 3 V versus Li/Li$^+$ at the ambient temperature with a multichannel Landt Battery Tester. Cyclic voltammetry (CV) tests were carried out between 0.01 and 3 V versus Li$^+$/Li with an Autolab electrochemical workstation (PGSTAT302N, Metrohm-Autolab).

TEM, ex situ and *in situ* TEM electrochemical characterizations. All TEM and scanning TEM (STEM) were performed using a JEOL JEM-2100F microscope operated at 200 kV, equipped with a Gatan Enfina electron spectrometer. Electron energy-loss spectroscopy (EELS) mapping was carried out under a 200 kV accelerating voltage with a 13 mrad convergence angle for the optimal probe condition. An energy dispersion of 0.7 eV per channel and a collection angle of 21 mrad were set for EELS, with high-angle annular dark field (HAADF) images acquired with an 89 mrad inner angle simultaneously. The Co and O elemental maps were extracted from the EELS spectrum image by integrating across the energy windows of 779-803 ($L_{2,3}$ edge) and 532-543 (K edge) eV, respectively. The elemental map for Li was extracted using multiple linear least squares fitting (MLLS) in the Digital Micrograph (Gatan, USA) software for solving the Li-K edge and Co-$M_{2,3}$ edge overlapping. The *ex situ* TEM experiments were performed using the TEM "grid in a coin cell" (**Figure S1**) set up using liquid electrolyte for

easy postmortem TEM characterizations. The *in situ* TEM experiments followed a similar design of the *in situ* cell as reported by Wang and co-workers.[26] The Co_3O_4 nanoarrays/nanosheets were loaded onto an electrochemically etched micro-size tungsten tip and fixed with conductive silver epoxy. Another tungsten tip with a submicron size at the end was used to scratch the fresh Li metal surface in an argon-filled glove box, and attached to a piezo-driven biasing probe built into the Nanofactory TEM scanning tunneling microscope (STM) holder. Before taking the holder into the ambient air, the holder tip was sealed by a plastic cap and then wrapped in a Parafilm tape. Once the sealed holder was taken out from the glovebox, it was inserted into the TEM column as quickly as possible for the *in situ* study of lithiation. The Li_2O on the Li metal surface serves as a solid electrolyte. Illustration videos of the *in situ* lithiation/delithiation processes of Co_3O_4 nanoarrays (Supporting information Video SI1-3) and nanosheets (Supporting information Video SI4) were taken and the corresponding dose rates (units of number of electrons per square ångström per second, $e^- \text{Å}^{-2} \cdot s^{-1}$) were ~ 122 and 78 $e^- \text{Å}^{-2} \cdot s^{-1}$ respectively.

3. RESULTS AND DISCUSSION

3.1. Preparation and Characterization of Co_3O_4 nanosheets and nanoarrays on carbon cloth

The morphologies of Co_3O_4 nanosheets and nanoarrays on carbon cloth (CC) substrates at different magnifications are revealed by scanning electron microscopy (SEM) images in **Figure 1**. **Figure 1a-b** show Co_3O_4 nanosheets homogeneously distributed over the whole CC substrate, forming a three-dimensional (3D) interconnected porous structure. The nanosheets have an average radical length (normal to the carbon fiber axis) of ~300 nm and axial widths (parallel to the carbon fiber axis) of ~900 nm. **Figure 1e-f** indicate that Co_3O_4 nanoarrays are in the bundle

form and densely cover the surface of CC, with an average length of ~4 μm and tapered with narrow tips. XRD (**Figure S2**) on nanosheets and nanoarrays confirms their phase to be Co_3O_4 spinel (JCPDS card No. 00-009-0418), with one additional broad peak at 25.3° coming from graphitized CC. TEM observation (**Figure 1c and 1g**) on the two nanostructures is also carried out. The selected area electron diffraction (SAED) (the inset of **Figure 1c and 1g**) and high-resolution TEM (HRTEM) (**Figure 1d and 1h**) consistently show the spinel phase of Co_3O_4 in both nanosheets and nanoarrays, whose chemical composition is further verified using electron energy-loss spectroscopy (EELS) in **Figure S3**. In combination with the XRD analysis, we thus are confident that two distinct nanostructures with the same spinel Co_3O_4 phase have been obtained. The Co_3O_4 nanosheets are mostly <110> oriented large crystals with nanopores in between, as determined from SAED and HRTEM, with the thickness ~7 nm measured from those inclined or perpendicular nanosheets (**Figure S4**). In contrast, the Co_3O_4 nanoarrays are polycrystalline with grain sizes of 3-40 nm. Combining both TEM and SEM observations, the dimensional differences between Co_3O_4 nanosheets and nanoarrays can be derived: the average widths of Co_3O_4 nanosheets and nanoarrays are ~900 nm vs. ~ 25 nm (tapered with narrow tips); the average lengths of Co_3O_4 nanosheets and nanoarrays are ~300 nm vs. ~4 μm.
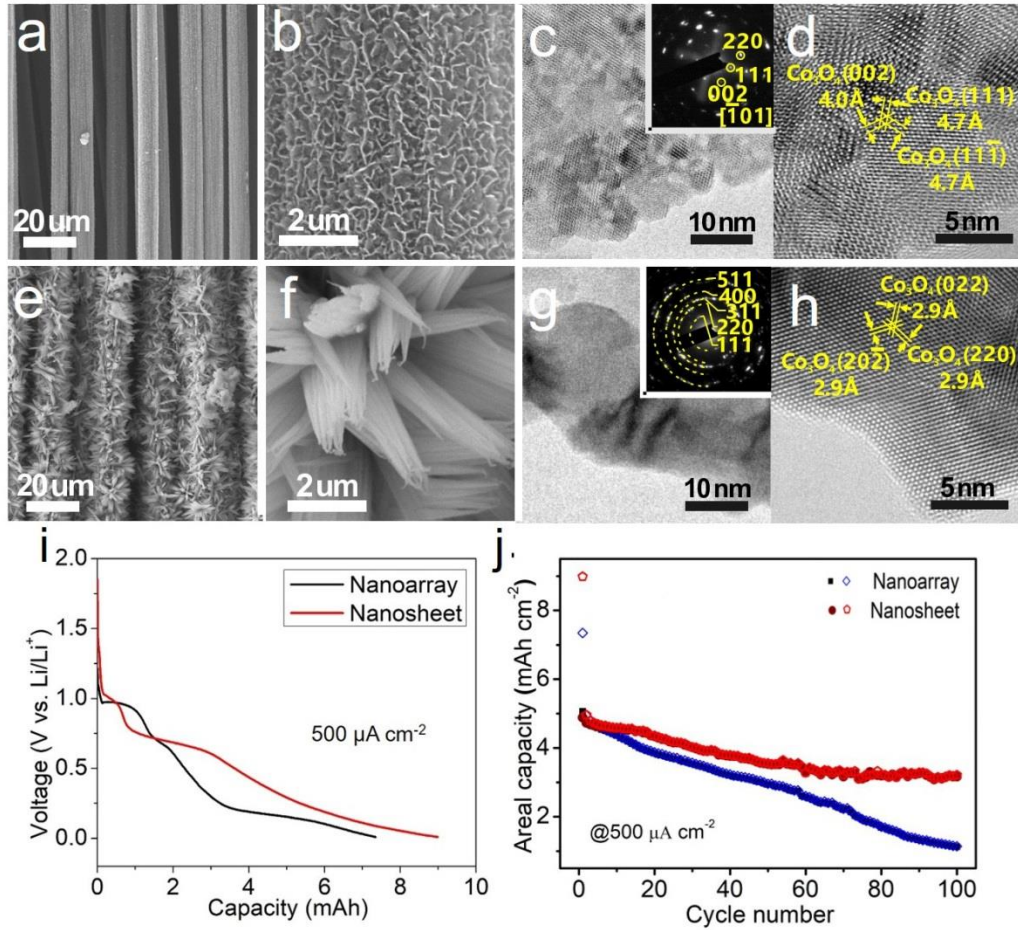
Figure 1. SEM images of CC@Co_3O_4 nanosheets (a-b) and CC@Co_3O_4 nanoarrays (e-f) at different magnifications. Comparison of high-magnification TEM images (c and g) and their corresponding SAED patterns (the inset of c and g) of Co_3O_4 nanosheets and nanoarrays. HRTEM images of Co_3O_4 nanosheets (d) and nanoarrays (h). (i) Voltage profile comparison of CC-based Co_3O_4 nanoarrays/nanosheets at the first cycle lithiation at the current density of 500 $\mu A\ cm^{-2}$. (j) Areal capacity-cycle plots of Co_3O_4 nanosheets (hollow red pentagon: discharge; dark red circle: charge) and nanoarrays (hollow blue rhomb: discharge; dark square: charge) obtained at the current density of 500 $\mu A\ cm^{-2}$.

The successful fabrication of the two kinds of Co_3O_4 nanostructures enables us to investigate the effect of morphologies (shape and crystallinity) on LIB performance. 2032-type

coin cells using CC-based Co_3O_4 nanoarrays/nanosheets as anodes are fabricated. Through a comparison of voltage profiles of CC-based Co_3O_4 nanoarrays/nanosheets (**Figure 1i**) at the first cycle lithiation with that of CC (**Figure S5**), we find out that lithiation of Co_3O_4 nanosheets presents a sloping discharge profile without obvious plateau regions, while an evident plateau region at around 1.0 V exists for the lithiation of Co_3O_4 nanoarrays, indicating their different lithiation dynamics. Galvanostatic charge-discharge measurements (**Figure 1j**) are carried out to compare the capacities of the two kinds of electrodes upon cycling. With the initial lithiation capacity of ~9.0 mAh cm^{-2} and ~7.3 mAh cm^{-2} for CC@Co_3O_4 nanoarrays and CC@Co_3O_4 nanosheets, respectively, the initial reversible capacity of both CC@Co_3O_4 nanoarrays and CC@Co_3O_4 nanosheets is ~5 mAh cm^{-2}. With almost the same initial reversible capacity (~5 mAh cm^{-2}), the CC@Co_3O_4 nanosheets anode maintains a capacity of ~3.2 mAh cm^{-2} after 100th cycles, much higher than the CC@Co_3O_4 nanoarrays (~1.2 mAh cm^{-2}). We further deduct the areal capacity contribution from CC (**Figure S6**) and calculate the specific capacity-cycle plots within the first 50 cycles (**Figure S7**). It can be seen that with the significantly higher initial specific capacity of 2162 mAh g^{-1}, Co_3O_4 nanosheets also show a higher capacity retention with the specific capacity of 1182 mAh g^{-1} at the 50th cycle. Interestingly, the value of specific capacity of Co_3O_4 nanosheets at the 50th cycle still surpasses the theoretical capacity of Co_3O_4 (890 mAh g^{-1}), which is attributed to the strong surface capacitance on Co^0 particles formed during discharge at low potentials[27]. The specific capacity of Co_3O_4 nanosheets is much higher than Co_3O_4 nanoarrays with specific capacity as low as 241 mAh g^{-1}. Such an improved electrochemical property from nanostructure engineering has been observed by others,[28] while the underlying mechanism remains largely unknown. Meanwhile, even though the mass loading of Co_3O_4 nanosheets and Co_3O_4 nanoarrays is different, morphology effect on lithiation

behaviors can still be observed through ex situ/in situ TEM and ex situ XRD characterizations, which will be further clarified later.

3.2. Effect of Nanostructures on Cycling Stability of Co_3O_4

To investigate the structural and phase evolution during lithiation/delithiation cycles, we set up the open-cell configuration of the *in situ* LIB[29-30] inside a TEM, as illustrated in **Figure S8** and described in detail in Experimental Section, which can offer high spatial resolution imaging and real-time analytical capabilities. Since the phase evolution of one sole nanoarray/nanosheet is observed, the distinct mass loading of Co_3O_4 nanosheets and Co_3O_4 nanoarrays on 1 cm^2 carbon cloth does not affect the comparison. With the contact established between the Li/Li_2O counter electrode and Co_3O_4 nanosheets/nanoarrays, a -1 V bias voltage is applied to drive the flow of electrons and Li^+ ions across the circuit, initiating the electrochemical lithiation in Co_3O_4 nanosheets/nanoarrays, while a +7 V bias is applied to initiate the delithiation process. To illustrate the lithiation/delithiation cycling of Co_3O_4 nanoarrays (**Supporting information Video SI1**), we have selected one segment in a Co_3O_4 nanoarray between two reference positions of A and B (L_a) (**Figure 2a**), with an initial length of 65 nm (L_0) and an initial diameter of 25 nm (d_0; the diameter d is defined as the average of the two marked diameters d_1 and d_2). Both d and L_a values during the first 6 lithiation/delithiation cycles are measured (**Figure 2b-l**) and summarized in **Table S1**, with the largest elongation L_a~102 nm corresponding to the elongation rate R_{ea}=57%. We then derive the volume of the nanoarray segment based on the expression $\frac{\pi d^2}{4} \times L$ and the volume variation ratio (R_{va}) through dividing volume increments by the original volume (V_0), as plotted in **Figure 2n** (also summarized in **Table S1)**. The R_{va} value after the 1st cycle is as large as 130%, followed by a little contraction from subsequent delithiation. Interestingly, after the 2nd lithiation, the volume expands more (219%) than the first lithiation, which has also

11

been observed by Xu *et al* in CuO electrode.[31] This may be attributed to pore formation in Co$_3$O$_4$ nanoarrays.[32-33] The largest contraction occurs at the 4th delithiation (99%), and the breakage of the nanoarray is captured during the 6th delithiation (**Figure 2m and Supporting information Video SI2**). There are two possible reasons for the failure of the nanoarray. It may be caused by fusing. More possibly, it may be triggered by the microstructure defects correlated with localized stresses induced by the Li concentration gradients, as demonstrated previously.[34] With the more inhomogeneous Li distribution in Co$_3$O$_4$ nanoarrays than Co$_3$O$_4$ nanoarrays, which will be demonstrated by *ex situ* XRD characterizations later, the higher localized stresses will be resultant from the more obvious Li concentration gradients in Co$_3$O$_4$ nanoarrays, resulting in higher possibility of microstructure defects or even fracture. A similar trend has been observed on another Co$_3$O$_4$ nanoarray segment (**Figure S9, Table S2, Supporting information Video SI2**).
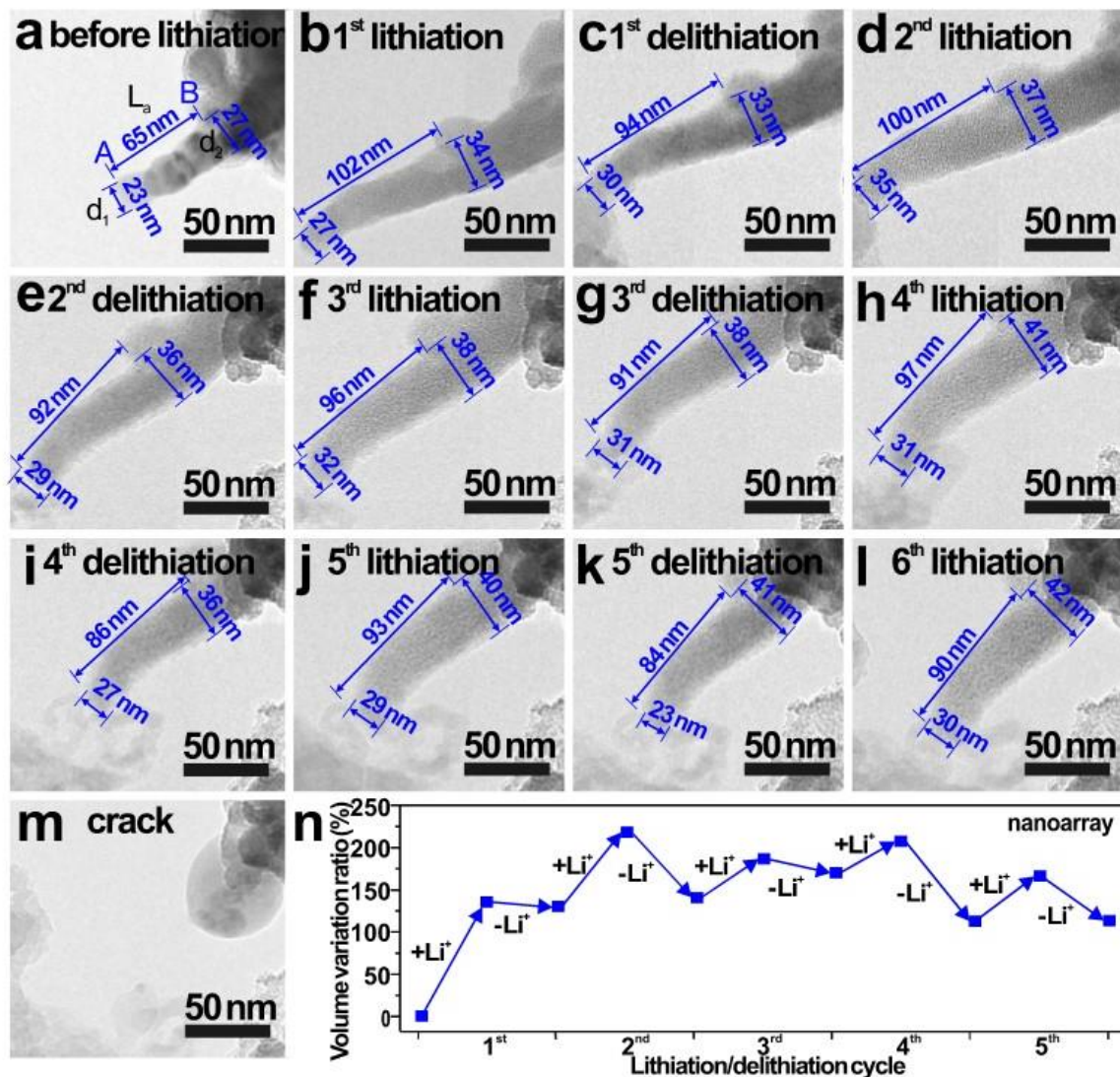
Figure 2. Microstructural evolution of a Co_3O_4 nanoarray in the *in situ* lithiation and delithiation cycles. (a) A pristine Co_3O_4 nanoarray. The lithiated (b, d, f, h, j and l) and delithiated (c, e, g, i, k and m) nanoarray after 1 to 6 cycles. (n) Volume variation ratios (R_{va}) over 5 lithiation/delithiation cycles.

In contrast, for Co_3O_4 nanosheets (**Supporting information Video SI3**), the effects of lithiation/delithiation cycling are also examined (**Figure 3a-f**). According to the TEM images, the porous sheet is found to transform to nonporous structure upon lithiation. The structural stability of the nanosheets are then studied through measuring the area change of the segment

13

defined by the two reference positions (C and D) and the contact position with metallic Li (E), since the measurement of the expansion in the thickness direction is a limitation of in situ TEM experiment. The original segment is 83 nm long and 217 nm wide with the length (L_s) and width (W) defined as the perpendicular distance from E to CD and the length of the CD line, respectively. After the first lithiation, W and L_s increase to 235 nm and 98 nm, respectively, with a broadening ratio (R_{bs}, **Table S3**) of 8.29% and an elongation ratio (R_{es}) of 18.1%, significantly smaller than that of nanoarrays (**Figure S10**). Based on the elongation ratio (R_{es} and R_{ea}) and the total lengths of nanosheets (18.1% and ~300 nm) and nanoarrays (57% and ~4000 nm), the average elongations are estimated as ~54 nm for Co_3O_4 nanosheets and ~2300 nm for nanoarrays (**Figure 3g**). Such a small elongation of nanosheets would be very much preferred by battery designers, to avoid piercing the separator in liquid-electrolyte LIBs, or to maintain a stable electrolyte/electrode interface in all-solid-state LIBs. After the first delithiation, W and L_s decrease to 223 and 87 nm, respectively, which increase only by 2.76% and 4.81% compared to the original dimensions. For the next two cycles, both R_{bs} and R_{es} closely follow the change of the first cycle, as summarized in **Table S3**. Using the method reported by Yu, et al[35], the volume expansion of Co_3O_4 nanosheets is calculated and compared with Co_3O_4 nanoarrays (**Figure 3h**). The volume of nanosheets expands marginally and reversibly at a maximum value of ~35% during three discharge/charge cycles, which is significantly smaller than that of nanoarrays (219% at maximum), suggesting its better cycling stability. Meanwhile, considering the better structural stability of Co_3O_4 nanosheets and the disappearance of porous structures at lithiation, the pores in nanosheets take part in accommodating the volume expansion of nanosheets, as demonstrated previously.[14]
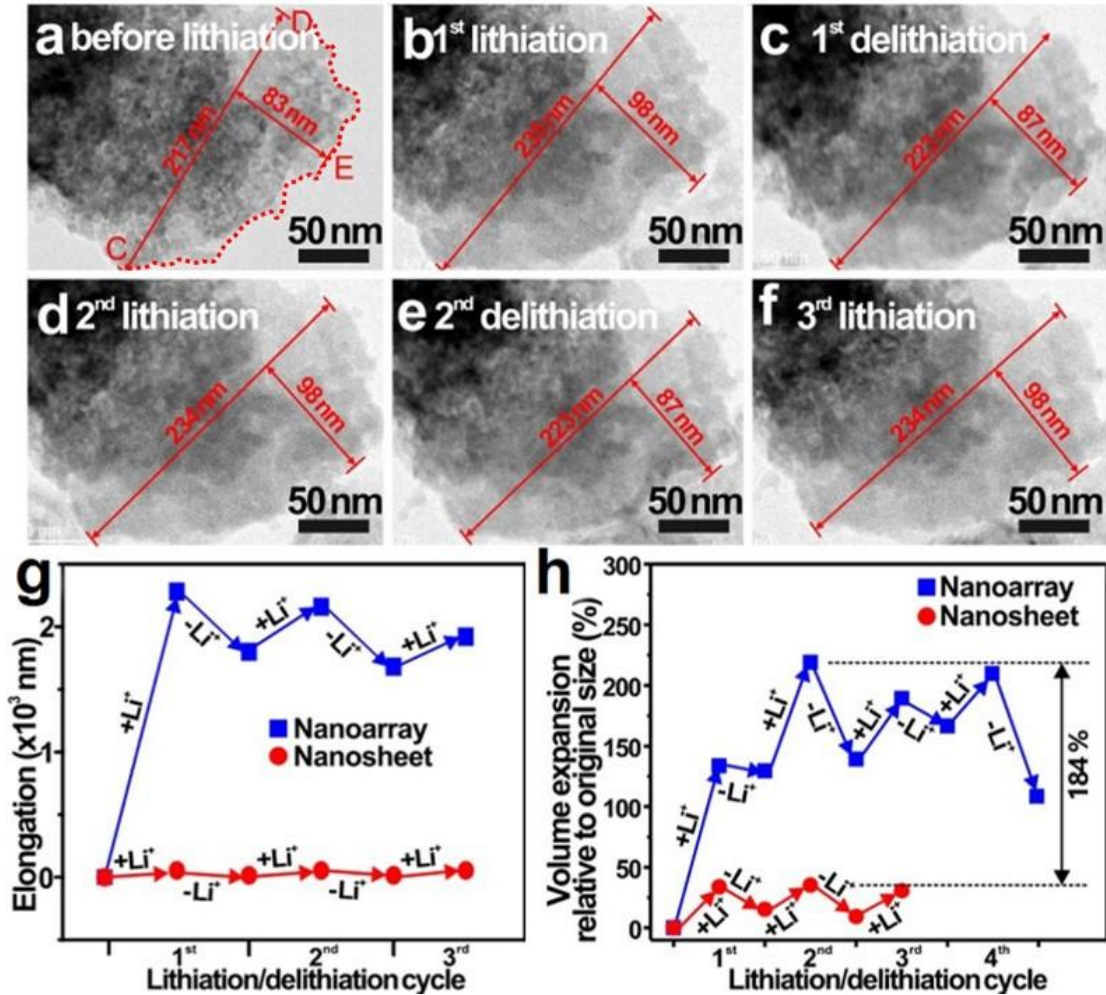
Figure 3. Microstructural evolution of a Co_3O_4 nanosheet in the *in situ* lithiation and delithiation cycles. (a) A pristine Co_3O_4 nanosheet. The lithiated (b, d and f) and delithiated (c and e) nanosheet after 1 to 3 cycles. (g) Comparison of elongations for nanoarrays and nanosheets. (h) Comparison of volume expansion relative to original size for Co_3O_4 nanoarray and nanosheet.

Phase evolution processes in Co_3O_4 nanosheets and nanoarrays after *in situ* lithiation/delithiation are analyzed according to element distribution in EELS maps (**Figure 4a-b**). In both nanostructures, higher concentration of Li (Li accumulation) is revealed at the surface, indicating large inhomogeneities[36] of Li distribution from surface to the center of the electrodes. It also verifies that lithiation predominantly occurs through surface diffusion,

resulting in higher lithiation kinetics in nanosheets than in nanorods. **Figure 4c** and **Figure S11** show *in situ* EEL spectra of nanosheets and nanoarrays allowing the direct comparison of Co $L_{2,3}$-edges and O K-edge at three different states: the pristine Co_3O_4, the lithiated, and the delithiated states. After lithiation, the Co $L_{2,3}$-edges (red curve) are shifted by $\sim$-1.5 eV compared with pristine Co_3O_4 (black curve), indicating the reduction of Co_3O_4 to Co^0 due to lithiation. The O K-edge (red curve) shows the characteristic peaks of Li_2O,[37] confirming the overall lithiation reaction: $Co_3O_4 + 8\ Li^+ + 8e^- \rightarrow 3Co + 4\ Li_2O$, which is further confirmed by the characteristic peak of Li K-edge at $\sim$ 58.5 eV attributed to the formation of Li_2O.[38] While after delithiation, the Co $L_{2,3}$-edges (blue curve) are shifted back by $\sim$1.0 eV (still $\sim$0.5 eV lower than the pristine Co_3O_4), showing that the phase after delithiation is CoO with the delithiation reaction: $Co + Li_2O \rightarrow CoO + 2Li^+ + 2e^-$. This is further verified by the O K-edge (blue curve) with considerably reduced prepeak intensity compared to the pristine Co_3O_4 (black curve), [39] and significantly decreased peak intensity of Li_2O peak. In addition, *in situ* SAED on nanosheets (**Figure 4d**) and nanoarrays (**Figure S12**) confirms the phase evolutions during lithiation/delithiation: while lithiation induces the phase change from Co_3O_4 to Co^0 and Li_2O, CoO is formed after delithiation instead of Co_3O_4. Obviously, the same phase evolution pathways found out by *in situ* TEM cannot explain the significant difference in the structural stability, which necessitates further characterizations.
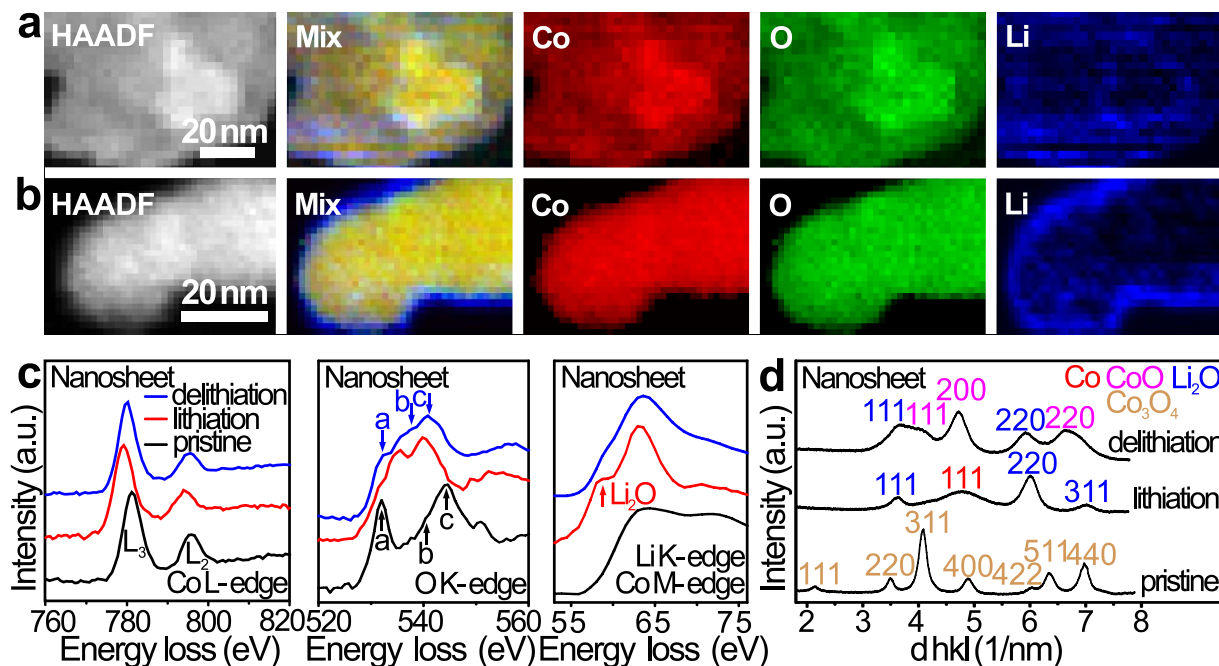
Figure 4. EELS elemental maps of the nanosheet (a) and the nanoarray (b) after lithiation. EEL spectra (c) and the radial-averaged intensity plot of SAED patterns (d) of Co_3O_4 nanosheets at the pristine, the lithiated, and the delithiated states.

3.3. Effects of Nanostructures on Lithiation Reaction Pathways of Co_3O_4.

To probe the detailed lithiation mechanism, phase evolution during the initial discharge is investigated through the combination of *ex situ* XRD and TEM characterizations. The experiment setup of "TEM grid in a coin cell" using liquid electrolyte[40] (**Figure S1**) is employed for postmortem TEM characterization and the samples grown on CC are used for *ex situ* XRD characterization. The discharge rate of 500 μAcm^{-2} is first used for *ex situ* studies, in order to be consistent with galvanostatic discharge/charge test. As shown in **Figure 5**, diffraction peaks related to cubic spinel Co_3O_4 are observed on fresh electrodes for both samples (purple curves, **Figure 5**). When discharged to 1.2 V (**Figure S13**), pristine Co_3O_4 nanosheets are fully converted to CoO as indicated by the appearance of CoO diffraction peaks at 36.3°, 42° and 61° (red curve, **Figure 5a**) and the disappearance of Co_3O_4 diffraction peaks at 36.8°, 59° and 65°.

This is further confirmed by *ex situ* TEM observation (**Figure S14**) showing the presence of rocksalt CoO phase after discharging at 1.2 V. When the electrode is further lithiated to 0.01 V (black curve, **Figure 5a and Figure S15**), diffraction peaks related to CoO disappear. Instead, the peak related to metallic Co^0 at 44° emerges, indicating the full conversion from CoO to Co^0. The large peak width is due to the formation of nanocrystalline Co^0 phase after the full conversion. Thus **Figure 5a** indicates the two-step lithiation in Co_3O_4 nanosheets, consistent with previous report:[18] $Co_3O_4 + 2Li^+ + 2e^- \rightarrow 3CoO + Li_2O$; $CoO + 2Li^+ + 2e^- \rightarrow Co + Li_2O$. In contrast, Co_3O_4 nanoarrays show negligible trace of CoO phase throughout the discharging process (**Figure 5b**). Instead, at 1.2 V (red curve, **Figure 5b and Figure S16**) diffraction peaks of Co_3O_4 (59° and 65°) remain together with diffraction peaks of Co^0 (44°), which indicates the coexistence of unlithiated and lithiated regions with the lithiated product of Co^0. Especially, even though the weakening XRD peak at 36.8° indicates phase evolution as lithiation progresses, the peak remains at the lithiated voltages of both 1.0 V (green curve, **Figure 5b and Figure S17**) and 0.01 V (black curve, **Figure 5b and Figure S18**) indicating the existence of unlithiated Co_3O_4. It thus can be concluded that one-step conversion from Co_3O_4 to Co^0 occurs in the initial lithiation of Co_3O_4 nanoarrays: $Co_3O_4 + 8Li^+ + 8e^- \rightarrow 3Co + 4Li_2O$. **Figure 5a** and **5b** unambiguously demonstrate two different lithiation paths mediated by the distinct nanostructures.
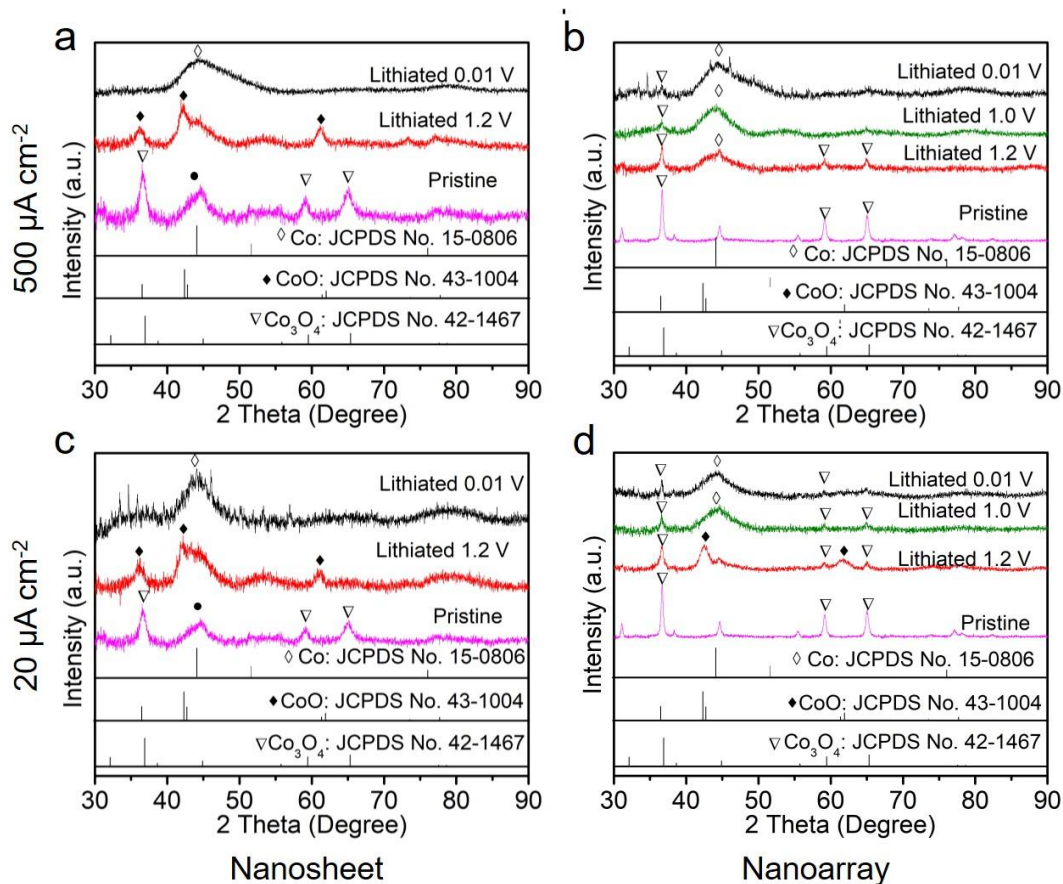
Figure 5. *Ex situ* XRD spectra of CC@Co$_3$O$_4$ nanosheets (a and c) and CC@nanoarrays (b and d) anodes lithiated to different voltages at charge/discharge rates of 500 μA cm^{-2} (a and b) and 20 μA cm^{-2} (c and d) during the initial cycle. The XRD signal of a Kapton film window used in *ex situ* XRD measurement is marked with black dots.

Such nanostructure-dependent lithiation path also depends on the discharge rate. At a low current density of 20 μA cm^{-2}, Co$_3$O$_4$ of both morphologies exhibits the two-step conversion (from Co$_3$O$_4$ to CoO to Co^0) according to the existence of CoO diffraction peaks at 36.3°, 42° and 61°. At 1.2 V, Co$_3$O$_4$ nanosheets (**Figure 5c and Figure S19**) still get fully converted to CoO, while the conversion of Co$_3$O$_4$ nanoarrays (**Figure 5d and Figure S21-S23**) is incomplete with the mixed lithiated phase of CoO and unlithiated phase of Co$_3$O$_4$, which has also been verified explicitly by *ex situ* TEM (**Figure S24**). When the CoO phase is further lithiated to form

the Co^0 phase at ≤1.0 V, there remains unlithiated Co_3O_4 (green and black curves, **Figure 5d and Figure S21-S23**). The formation of Co^0 phase at 0.01 V for Co_3O_4 nanosheets is confirmed by *ex situ* TEM (**Figure S25**). The consistency between the *ex situ* TEM and *ex situ* XRD characterization results show the negligible effect of the mass loading on the lithiation kinetics, considering the distinct mass loading of the *ex situ* TEM and *ex situ* XRD samples.
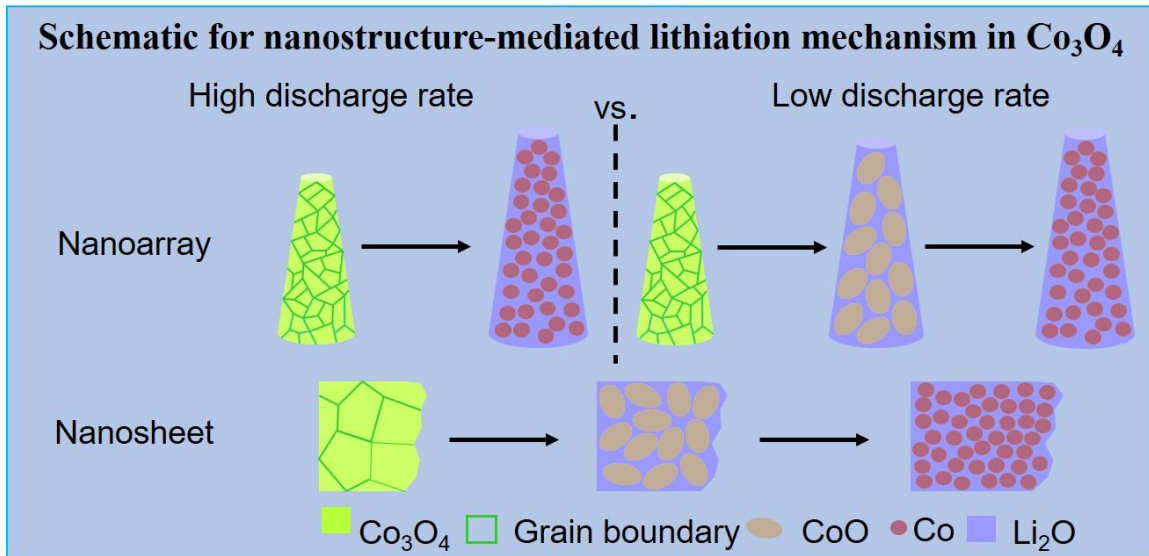
To confirm the driving/limiting force for nanostructure-mediated lithiation pathways, Li^+ transport speeds in both nanosheets and nanoarrays are derived from CV measurement to directly compare their lithiation kinetics.[41] **Figure 6a and 6b** show the CV curves for the CC-based Co_3O_4 nanoarrays and nanosheets, respectively. For both nanostructures, all peak currents increase with increasing scan rates, consistent with the diffusion-controlled process in which the peak currents are proportional to the square root of the scan rate.[42] The diffusion coefficients of Li^+ in Co_3O_4 nanosheets and nanoarrays can be further derived using the Randles-Sevick equation:[43] $i_p = 2.69 \times 10^5 n^{3/2} A D_{Li}^{1/2} C_{Li} v^{1/2}$, where i_p is the peak current in amps, n is the number of the electrons transferred, A is electrode area in cm^2, v is the scan rate in V s^{-1}, and D_{Li} and C_{Li} are the diffusion coefficient in cm^2 s^{-1} and concentration of Li^+ in mol cm^{-3}. The peaks at ~0.85 V at the CV curves are equivalent to the characteristic peaks at ~1.2 V at the lithiation voltage curves, since different testing machines and conditions result in the polarization difference and the resultant distinct characteristic peaks at which phase change appears to take place. Through analyzing the slopes of the $i_p - v^{1/2}$ curves (**Figure 6c**) using cathodic peak currents at 0.85 V (with the cathodic peak currents of ~0.5 V[44-45] attributed to lithiation of carbon fiber), it can be found out that Co_3O_4 nanosheets show significantly faster lithiation kinetics than the nanoarrays.
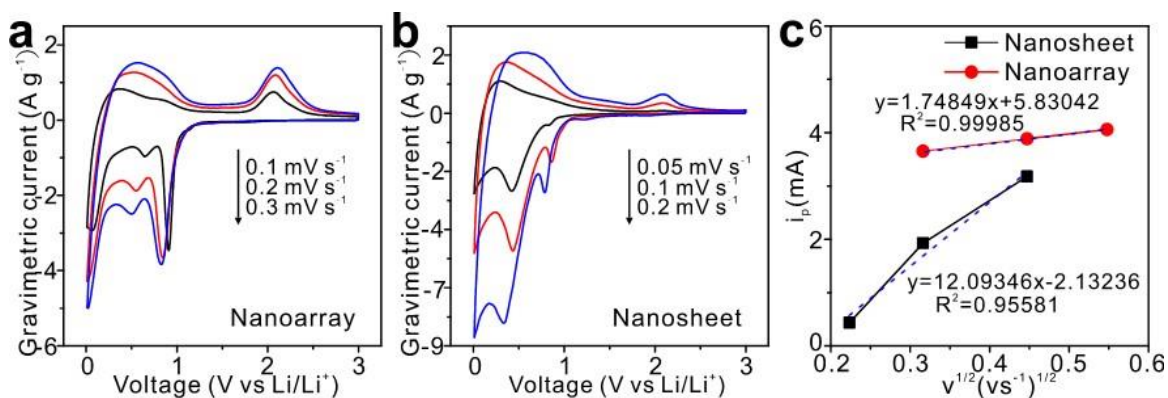
Figure 6. CV plots of CC-based Co_3O_4 nanoarrays (a) and nanosheets (b). (c) i_p-$v^{1/2}$ plots of two kinds of CC-based anodes using cathodic peak currents at 0.85 V.

Therefore, by combining the *ex-situ* XRD and CV results, nanostructure-mediated lithiation pathways can be explained as follows: due to the slow lithiation kinetics of Co_3O_4 nanoarrays, local Li^+ accumulation takes place, which is reflected by the coexistence of unlithiated Co_3O_4 and lithiated Co^0 phases in Co_3O_4 nanoarrays. When a high discharge rate is applied, rapid Li^+ accumulation results in localized sharp voltage drop at the reaction fronts, driving the one-step phase conversion from Co_3O_4 to Co^0. When a low discharge rate is applied, Li^+ has relatively sufficient time to achieve a gradual voltage drop in Co_3O_4 nanoarrays, and thus the two-step conversion occurs. For Co_3O_4 nanosheets, fast lithiation kinetics can avoid nanosheets from the issue of local Li^+ accumulation, which results in two step conversion reactions at both high and low discharge rates. Meanwhile, full lithiation always takes place in Co_3O_4 nanosheets, in obvious contrast to existence of unlithiated Co_3O_4 phases for Co_3O_4 nanoarrays even at the low discharge rate.

3.4. Proposed Mechanism

21

Schematic for nanostructure-mediated lithiation mechanism in Co$_3$O$_4$

High discharge rate vs. Low discharge rate

Nanoarray

Nanosheet

Co$_3$O$_4$ ☐ Grain boundary ● CoO ● Co ■ Li$_2$O

Figure 7. Proposed schematic to explain the effect of nanostructure on phase evolution for Co$_3$O$_4$ electrode.

By correlating ex situ XRD, (in situ/ex situ) TEM and electrochemical results, we can now propose a mechanism to help us understand how nanostructure affects lithium storage capability. Figure 7 presents a schematic on the proposed phase transformation process for different nanostructures. When the nanoarray is cycled at a high discharge rate, such as 500 μA cm^{-2}, there is not enough time for Li to fully lithiate all the active materials, indicated by the coexistence of lithiated and unlithiated Co$_3$O$_4$ nanoarrays, resulting in a low value of areal capacity. In addition, mixtures of phases and structures in Co$_3$O$_4$ nanoarrays (lithiated and unlithiated Co$_3$O$_4$) undergo different amounts of volume changes, and therefore, leads to nonuniform volume changes of Co$_3$O$_4$ nanoarray electrodes during lithiation and delithiation which causes stress to the electrode, resulting in structure failure and irreversible capacity loss. In contrast, due to the fast lithiation kinetics, the nanosheet experiences full lithiation from Co$_3$O$_4$ phase to CoO phase and then to Co phase when cycled at a high discharge rate, which results in delivery of high capacity. Meanwhile, full conversion from one phase (such as Co$_3$O$_4$) to the other phase (such as CoO) at

lithiation prevents the electrode from high interior stress, resulting in high cycling stability. When the nanoarray is cycled at a low discharge rate, such as 20 μA cm^{-2}, even though the two-step conversion reaction facilitates the slow relaxation of interior stress in nanoarray, the existence of unlithiated Co_3O_4 phase will still result in the delivery of a lower capacity than nanosheet.

4. CONCLUSIONS

In summary, we demonstrate explicitly the dependence of lithiation mechanism on Co_3O_4 nanostructures by unraveling and comparing the microscopic lithiation/delithiation behaviors of Co_3O_4 nanoarrays and nanosheets, which also explains the existing controversy in literature. The root cause of the nanostructure dependence is identified to be different lithiation kinetics intrinsic to the two nanostructures, with slower kinetics leading to one-step conversion in Co_3O_4 nanoarrays at high discharge rates, in contrast to the two-step conversion in Co_3O_4 nanosheets with higher lithiation kinetics. Furthermore, *in situ* TEM reveals larger volume change in Co_3O_4 nanoarrays, which in coupling with the slow lithiation kinetics raises internal stress during cycling and eventually causes fracture and irreversible capacity loss, while high structural reversibility and low interior stress of Co_3O_4 nanosheets contribute to the high cycling stability and capacity retention, facilitated by the fast lithiation kinetics. Overall, this work provides important insights into the interplay among lithiation kinetics, phase evolution and lithium storage performance which can be translated into electrode design strategies for next generation LIBs.

ASSOCIATED CONTENT

Four videos (avi) showing morphological change in two Co_3O_4 nanoarrays and a Co_3O_4 nanosheet, and sudden breakage of a nanoarray at the 6th discharge/charge cycles. Further information concerning three tables for the summary of the morphological change for the reference positions in two Co_3O_4 nanoarrays and one Co_3O_4 nanosheet, some snapshots from supporting information Video SI3 showing microstructural evolution of another Co_3O_4 nanoarray, specific capacity-cycle plots of Co_3O_4 nanosheets and nanoarrays, areal capacity-cycle plots of CC, voltage profiles of CC, CC@Co_3O_4 nanoarrays and CC@Co_3O_4 nanosheets lithiated to different voltages, TEM and HRTEM images of Co_3O_4 nanosheets at the lithiated voltage of 1.2 V with the current density of 500 $\mu A\ cm^{-2}$ and at the lithiated voltage of 0.01 V with the current density of 20 $\mu A\ cm^{-2}$, TEM and HRTEM images of Co_3O_4 nanoarrays at the lithiated voltage of 1.2 V at the current density of 20 $\mu A\ cm^{-2}$, XRD patterns of Kapton films, the experiment setup of "TEM grid in a coin cell", fast fourier transform (FFT) patterns of Co_3O_4 nanoarrays and nanosheets and also EELS spectra and SAED diffraction patterns of Co_3O_4 nanoarrays at three different states: the pristine, the lithiated, and the delithiated state, and comparison of unit elongation ratios of nanoarrays and nanosheets as well as comparison of reaction front migration speed of nanoarrays and nanosheets can be found in the supplementary pdf. This material is available free of charge *via* the Internet at http://pubs.acs.org.

AUTHOR INFORMATION

Corresponding Author

*Limin Zhou. E-mail: zhoulm@sustech.edu.cn; *Ye Zhu. E-mail: yezhu@polyu.edu.hk

Author Contributions

‡These authors contributed equally. The manuscript was written through contributions of all authors. All authors have given approval to the final version of the manuscript.

Notes

The authors declare no competing financial interest.

REFERENCES

[1] Goodenough, J. B.; Park, K.-S. The Li-Ion Rechargeable Battery: A Perspective J. Am. Chem. Soc 2013, 135, 1167-1176.

[2] Whittingham, M. S. Electrical Energy Storage and Intercalation Chemistry Science 1976, 192, 1126-1127.

[3] Poizot, P.; Laruelle, S.; Grugeon, S.; Dupont, L.; Tarascon, J. M. Nano-Sized Transition-Metal Oxides as Negative-Electrode Materials for Lithium-Ion Batteries Nature 2000, 407, 496-499.

[4] Poizot, P.; Laruelle, S.; Grugeon, S.; Dupont, L.; Tarascon, J. M. From the Vanadates to 3d-Metal Oxides Negative Electrodes Ionics 2000, 6, 321-330.

[5] Hao, J.; Zhang, J.; Xia, G.; Liu, Y.; Zheng, Y.; Zhang, W.; Tang, Y.; Pang, W.; Guo, Z. Heterostructure Manipulation via in Situ Localized Phase Transformation for High-Rate and Highly Durable Lithium Ion Storage ACS Nano 2018, 12, 10430-10438.

[6] Zhao, Y.; Li, X. F.; Yan, B.; Xiong, D. B.; Li, D. J.; Lawes, S.; Sun, X. L. Recent Developments and Understanding of Novel Mixed Transition-Metal Oxides as Anodes in Lithium Ion Batteries Adv. Energy Mater. 2016, 6, 19.

[7] Li, C.; Chen, T. Q.; Xu, W. J.; Lou, X. B.; Pan, L. K.; Chen, Q.; Hu, B. W. Mesoporous Nanostructured Co_3O_4 Derived from MOF Template: a High-Performance Anode Material for Lithium-Ion Batteries J. Mater. Chem. A 2015, 3, 5585-5591.

[8] Wang,Y.; Xia, H.; Lu, L.; Lin, J. Y. Excellent Performance in Lithium-Ion Battery Anodes: Rational Synthesis of $Co(CO_3)(0.5)(OH)0.11H(2)O$ Nanobelt Array and Its Conversion into Mesoporous and Single-Crystal Co_3O_4 ACS Nano 2010, 4, 1425-1432.

[9] Nam, K. M.; Shim, J. H.; Han, D.-W.; Kwon, H. S.; Kang, Y.-M.; Li, Y.; Song, H.; Seo, W. S.; Park, J. T. Syntheses and Characterization of Wurtzite CoO, Rocksalt CoO, and Spinel Co_3O_4 Nanocrystals: Their Interconversion and Tuning of Phase and Morphology Chem. Mater. 2010, 22, 4446-4454.

[10] Zheng, M.; Tang, H.; Li, L.; H, Q.; Zhang, L.; Xue, H.; P, H. Hierarchically Nanostructured Transition Metal Oxides for Lithium-Ion Batteries Adv. Sci. 2018, 5, 1700592 .

[11] Li, Y.; Tan, B.; Wu, Y. Mesoporous Co_3O_4 Nanowire Arrays for Lithium-Ion Batteries with High Capacity and Rate Capability Nano Lett. 2008, 8, 265-270.

[12] Lai, L.; Zhu, J.; Li, Z.; Yu, D. Y. W.; Jiang, S.; Cai, X.; Yan, Q.; Lam, Y. M.; Shen, Z.; Lin, J. Co_3O_4/Nitrogen Modified Graphene Electrode as Li-Ion Battery Anode with High Reversible Capacity and Improved Initial Cycle Performance Nano Energy 2014, 3, 134-143.

[13] Wang, J.; Yang, N.; Tang, H.; Dong, Z.; Jin, Q.; Yang, M.; Kisailus, D.; Zhao, H.; Tang, Z.; Wang, D. Accurate Control of Multishelled Co_3O_4 Hollow Microspheres as High-Performance Anode Materials in Lithium-Ion Batteries Angew. Chem. Int. Ed. 2013, 52, 6417-6420.

[14] Fang, G.; Zhou, J.; Liang, C.; Pan, A.; Zhang, C.; Tang, Y.; Tan, X.; Liu, J.; Liang, S. MOFs Nanosheets Derived Porous Metal Oxide-Coated Three-Dimensional Substrates for Lithium-Ion Battery Applications Nano Energy 2016, 26, 57-65.

[15] Li, H.-H.; Zhou, L.; Zhang, L.-L.; Fan, C.-Y.; Fan, H.-H.; Wu, X.-L.; Sun, H.-Z.; Zhang, J.-P. Co_3O_4 Nanospheres Embedded in a Nitrogen-Doped Carbon Framework: An Electrode with Fast Surface-Controlled Redox Kinetics for Lithium Storage ACS Energy Lett. 2017, 2, 52-59.

[16] Hou, Y.; Li, J.; Wen, Z.; Cui, S.; Yuan, C.; Chen, J. Co_3O_4 Nanoparticles Embedded in Nitrogen-Doped Porous Carbon Dodecahedrons with Enhanced Electrochemical Properties for Lithium Storage and Water Splitting Nano Energy 2015, 12, 1-8.

[17] Thackeray, M. M.; Baker, S. D.; Adendorff, K. T.; Goodenough, J. B. Lithium Insertion into Co_3O_4: a Preliminary Investigation Solid State Ionics 1985, 17, 175-81.

[18] Zhang, J.; Jiang, H.; Zeng, Y.; Zhang, Y.; Guo, H. Oxygen-Defective Co_3O_4 for Pseudo-Capacitive Lithium Storage J. Power Sources 2019, 439, 227026.

[19] Chang, J. H.; Cheong, J. Y.; Kim, S. J.; Shim, Y.-S.; Park, J. Y.; Seo, H. K.; Dae, K. S.; C.-W.; Lee, I.-D.; Kim, J. M.; Yuk Graphene Liquid Cell Electron Microscopy of Initial Lithiation in Co_3O_4 Nanoparticles ACS Omega 2019, 4, 6784-6788.

[20] Li, J.; He, K.; Meng, Q. P.; Li, X.; Zhu, Y. Z.; Hwang, S; Sun, K.; Gan, H.; Zhu, Y. M.; Mo, Y. F.; Stach, E. A.; Su, D. Kinetic Phase Evolution of Spinel Cobalt Oxide during Lithiation ACS Nano 2016, 10, 9577-9585.

[21] Chae, B. M.; Oh, E. S.; Lee, Y. K. Conversion Mechanisms of Cobalt Oxide Anode for Li-Ion Battery: In Situ X-ray Absorption Fine Structure Studies J. Power Sources 2015, 274, 748-754.

[22] Lu, Y.; Wang, Y.; Zou, Y.; Jiao, Z.; Zhao, B.; He, Y.; Wu, M. Macroporous Co_3O_4 Platelets with Excellent Rate Capability as Anodes for Lithium-Ion Batteries Electrochem. Commun. 2010, 12, 101-105.

[23] Kang, Y.-M.; Song, M.-S.; Kim, J.-H.; Kim, H.-S.; Park, M.-S.; Lee, J.-Y.; Liu, H. K.; Dou, S. X. A Study on the Charge–Discharge Mechanism of Co_3O_4 as an Anode for the Li Ion Secondary Battery Electrochim. Acta 2005, 50, 3667-3673.

[24] Larcher, D.; Sudant, G.; Leriche, J.; Chabre, Y.; Tarascon, J. The Electrochemical Reduction of Co_3O_4 in a Lithium Cell J. Electrochem. Soc. 2002, 149, A234.

[25] Xu, W.; Chen, J.; Yu, M.; Zeng, Y.; Long, Y.; Lu, X.; Tong, Y. Sulphur-Doped Co_3O_4 Nanowires as an Advanced Negative Electrode for High-Energy Asymmetric Supercapacitors J. Mater. Chem. A 2016, 4, 10779-10785.

[26] Li, Y.; Liu, Z.; Cheng, X.; Liu, X.; Zhang, B.; Sun, D.; Wang, R.; Zhang, Y. Assembled Graphene Nanotubes Decorated by Hierarchical MoS_2 Structures: Enhanced Lithium Storage and In-Situ TEM Lithiation Study Energy Stor. Mater. 2017, 9, 188-194.

[27] Li, Q.; Li, H.; Xia, Q.; Hu, Z.; Moodera, J. S. Extra Storage Capacity in Transition Metal Oxide Lithium-Ion Batteries Revealed by In-Situ Magnetometry Nat. Mater. 2020, 1-8.

[28] Zhang,Y. Q.; Wu, Y. W.; Chu, Y. H.; Li, L.; Yu, Q. P.; Zhu, Y. F.; Liu, G.; Hou, Q.; Zeng, R. H.; Zhao, L. Z. Self-Assembled Co_3O_4 Nanostructure with Controllable Morphology towards High Performance Anode for Lithium Ion Batteries Electrochim. Acta 2016, 188, 909-916.

[29] Fan, Z.; Zhang, L.; Baumann, D.; Mei, L.; Yao, Y.; Duan, X.; Shi, Y.; Huang, J.; Huang, Y.; Duan, X. In Situ Transmission Electron Microscopy for Energy Materials and Devices Adv. Mater. 2019, 31, 1900608.

[30] Xu, Z.-L.; Zhang, B.; Gang, Y.; Cao, K.; Garakani, M. A.; Abouali, S.; Huang, J.; Huang, J.-Q.; Heidari, E. K.; Wang, H.; Kim, J.-K. In-Situ TEM Examination and Exceptional Long-Term Cyclic Stability of Ultrafine Fe_3O_4 Nanocrystal/Carbon Nanofiber Composite Electrodes Energy Stor. Mater. 2015, 1, 25-34.

[31] Su, Q.; Yao, L.; Zhang, J.; Du, G.; Xu, B. In Situ Transmission Electron Microscopy Observation of the Lithiation–Delithiation Conversion Behavior of CuO/Graphene Anode ACS Appl. Mater. Interfaces 2015, 7, 23062-23068.

[32] Boebinger, M. G.; Yarema, O.; Yarema, M.; Unocic, K. A.; Mcdowell, M. T. Spontaneous and Reversible Hollowing of Alloy Anode Nanocrystals for Stable Battery Cycling Nat. Nanotechnol. 2020, 15, 475.

[33] Liu, X. H.; Huang, S.; Picraux, S. T.; Li, J.; Zhu, T.; Huang, J. Y. Reversible Nanopore Formation in Ge Nanowires during Lithiation–Delithiation Cycling: An In Situ Transmission Electron Microscopy Study Nano Lett. 2011, 11, 3991–3997.

[34] Bi, Y.; Tao, J.; Wu, Y.; Li, L.; Xu, Y.; Hu, E.; Wu, B.; Hu, J,; Wang, C.; Zhang, J.; Qi, Y.; Xiao, J. Reversible Planar Gliding and Microcracking in a Single-Crystalline Ni-Rich Cathode Science. 2020, 370, 1313-1317.

[35] Chen, D.; Peng, L.; Yuan, Y.; Zhu, Y.; Fang, Z.; Yan, C.; Chen, G.; hahbazian-Yassar, R.; Lu, J.; Amine, K.; Yu, G. Two-Dimensional Holey Co_3O_4 Nanosheets for High-Rate Alkali-Ion Batteries: From Rational Synthesis to in Situ Probing Nano Lett. 2017, 17, 3907-3913.

[36] Jo, E.; Hwang, S.; Kim, S.; Chang, W. Investigating the Kinetic Effect on Structural Evolution of $Li_xNi_{0.8}Co_{0.15}Al_{0.05}O_2$ Cathode Materials during the Initial Charge/Discharge Chem. Mater. 2017, 29, 2708.

[37] Qiao, R.; Chuang, Y. D.; Yan, S.; Yang, W. Soft X-Ray Irradiation Effects of Li_2O_2, Li_2CO_3 and Li_2O Revealed by Absorption Spectroscopy PloS One 2012, 7, e49182.

[38] Wang, F.; Graetz, J.; Moreno, M. S.; Ma, C.; Wu, L. J.; Volkov, V.; Zhu, Y.M. Chemical Distribution and Bonding of Lithium in Intercalated Graphite: Identification with Optimized Electron Energy Loss Spectroscopy ACS Nano 2011, 5, 1190–1197.

[39] Zhao, Y.; Feltes, T. E.; Regalbuto, J. R.; Meyer, R. J.; Klie, R. F. In Situ Electron Energy Loss Spectroscopy Study of Metallic Co and Co Oxides J. Appl. Phys. 2010, 108, 1.

[40] Lin, F.; Nordlund, D.; Weng, T.-C.; Zhu, Y.; Ban, C.; Richards, R. M.; Xin, H. L. Phase Evolution for Conversion Reaction Electrodes in Lithium-Ion Batteries Nat. Commun. 2014, 5, 3358.

[41] Lim, L.Y., Fan, S.; H. H.; Toney, M. F. Storage Capacity and Cycling Stability in Ge Anodes: Relationship of Anode Structure and Cycling Rate Adv. Energy Mater. 2015, 5, 91.

[42] Fu, F.; Yao, Y.; Wang, H.; Xu, G.-L.; Amine, K.; Sun, S.-G.; Shao, M. Structure Dependent Electrochemical Performance of Li-Rich Layered Oxides in Lithium-Ion Batteries Nano Energy 2017, 35, 370-378.

[43] Jung, H.-G.; Hassoun, J.; Park, J.-B.; Sun,Y.-K.; Scrosati, B. An Improved High-Performance Lithium–Air Battery Nat. Chem. 2012, 4, 579-585.

[44] Balogun, M. S.; Li, C.; Zeng, Y.; Yu, M.; Wu, Q.; Wu, M.; Lu, X.; Tong, Y. Titanium Dioxide@Titanium Nitride Nanowires on Carbon Cloth with Remarkable Rate Capability for Flexible Lithium-Ion Batteries J. Power Sources, 2014, 272, 946-953.

[45] Liu, T.; Wang, W.; Yi, M.; Chen, Q.; Xu, C.; Cai, D.; Zhan, H. Metal-Organic Framework Derived Porous Ternary $ZnCo_2O_4$ Nanoplate Arrays Grown on Carbon Cloth as Binder-Free Electrodes for Lithium-Ion Batteries Chem. Eng. J. 2018, 354, 454-462.

Graphical abstract
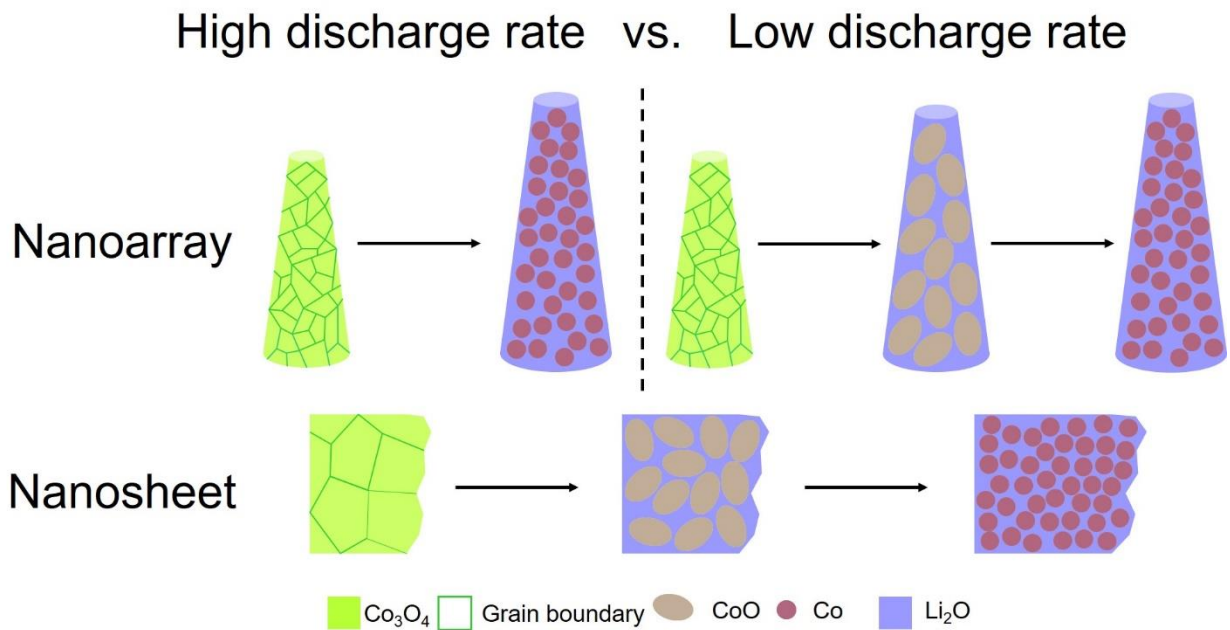
An in-depth mechanistic study on the influence of novel Co_3O_4 nanostructures on LIB performance is conducted. Different conversion reactions resulting from different Co_3O_4 nanostructures are for the first time revealed. This work not only explains the existing controversy about multi-step/single-step conversion reactions in Co_3O_4 anodes, but also provides critical insight towards nanostructure optimization for better LIB performance.